2D simulations of transport dynamics during tokamak fuelling by supersonic molecular beam injection

2014 Nucl. Fusion 54 043019

(http://iopscience.iop.org/0029-5515/54/4/043019)

IOP Publishing | International Atomic Energy Agency Nuclear Fusion
Nucl. Fusion **54** (2014) 043019 (16pp) doi:10.1088/0029-5515/54/4/043019

2D simulations of transport dynamics during tokamak fuelling by supersonic molecular beam injection

Z.H. Wang[1,2], X.Q. Xu[2], T.Y. Xia[1,3] and T.D. Rognlien[2]

[1] Southwestern Institute of Physics, Chengdu 610041, People's Republic of China
[2] Lawrence Livermore National Laboratory, Livermore, CA 94550, USA
[3] Institute of Plasma Physics, Chinese Academy of Sciences, Hefei 230031, People's Republic of China

E-mail: zhwang@swip.ac.cn

Received 11 August 2013, revised 16 January 2014
Accepted for publication 11 February 2014
Published 20 March 2014

Abstract

Time-dependent transport of both plasma and neutrals is simulated during supersonic molecular beam injection (SMBI) yielding the evolution of edge plasma and neutral profiles. The SMBI model is included as a module, called *trans-neut*, within the original BOUT++ boundary plasma turbulence code. Results of calculations are reported for the realistic divertor geometry of the HL-2A tokamak. The model can also be used to study the effect of gas puffing. A seven-field fluid model couples plasma density, heat, and momentum transport equations together with neutral density and momentum transport equations for both molecules and atoms. Collisional interactions between molecules, atoms, and plasma include dissociation, ionization, recombination and charge-exchange effects. Sheath boundary conditions and particle recycling are applied at both the wall and the divertor plates. A localized boundary condition of constant molecular flux (product of density times speed) is applied at the outermost flux surface to model the SMBI. Steady state profiles with and without particle recycling are achieved before SMBI. During SMBI, the simulation shows that neutrals can penetrate several centimetres inside the last closed (magnetic) flux surface (LCFS). Along the SMBI path, plasma density increases while plasma temperature decreases. The molecule penetration depth depends on both the SMBI flux and the initial plasma density and temperature along its path. As the local plasma density increases substantially, molecule and atom penetration depths decrease due to their higher dissociation and ionization rates if the electron temperature does not drop too low. Dynamic poloidal spreading of the enhanced plasma density region is observed due to rapid ion flow along the magnetic field (parallel) driven by a parallel pressure asymmetry during SMBI. Profile relaxation in the radial and poloidal directions is simulated after SMBI termination, showing that the plasma returns to pre-SMBI conditions on a time scale of 60 ms.

Keywords: plasma fueling, SMBI simulation, neutrals transport, penetration depth

(Some figures may appear in colour only in the online journal)

1. Introduction

Plasma fuelling with higher efficiency and deeper injection is crucial to enable fusion power performance requirements at high density for next generation devices such as ITER. There are three major fuelling methods: gas puffing (GP) [1], pellet injection (PI) [2] and supersonic molecular beam injection (SMBI) [3]. The fuelling efficiency of GP is low because its injection depth is usually very shallow and most molecules are localized outside the magnetic separatrix (last closed flux surface—LCFS) near the edge of tokamak. Pellets can be injected much deeper into the core plasma due to their much higher directed velocities and being large, condensed-matter objects. However, PI is more costly, requiring more complex techniques and equipment than GP. Thus, a new method of plasma fuelling that has higher fuelling efficiency compared to GP but costs less than PI is highly desirable. SMBI, which was first developed in the HL-1M tokamak and then widely applied in many other devices, has already been shown to be an improvement over conventional GP and also a comparable fuelling method to PI because of its directed higher injection speed, smaller angular distribution of particles, and stronger fuelling intensity than GP. Thus, SMBI enhances the particle injection depth and fuelling efficiency compared to GP, and its injection depth is also comparable to a small or low energy PI but costs less than a PI. There have been many experimental studies [3–5] to improve the penetration depth and fuelling efficiency of SMBI in the HL-2A tokamak, such as

changing from low (magnetic) field side (LFS) injection to high (magnetic) field side (HFS) injection, varying the injection speed, temperature, and particle flux intensity. Besides being a fuelling method, SMBI is also a good tool for plasma density control [5], L–H transition and confinement improvements [6], edge localized mode (ELM) mitigation [7], and nonlocal heat transport [8] studies.

It is critical to understand the physics and transport dynamics during the plasma fuelling process to guide research into methods to improve fuelling efficiency and injection depth. There are many key issues influencing fuelling particle transport that well understood, such as interactions between fuelling particles (deuterium and tritium) and the pre-injection plasma, loss rates of fuelling particles via complex collision reactions (i.e. ablation, dissociation, ionization, charge exchange), and influence of the plasma density rise along the injection path on fuelling particle propagation. Compared to PI [9], which involves ablation of highly condensed matter with bound states, SMBI is more like GP but with a directed high injection speed (i.e. convection dominated process). SMBI has a directed high injection speed in a range of 500–1200 m s^{-1} but a very low temperature (the room temperature 293 K $\approx$ 300 K). The transport of molecules during SMBI is dominated by convection rather than diffusion (e.g., GP), and SMBI involves interaction of unbound particles with plasma rather than an ablation and shielding dominated process (e.g., PI). Thus, SMBI should be modelled differently from both GP and PI. There are many neutral transport models of fuelling such as convection-ablation model of PI [9–11] and diffusion model of GP [12–14], but there is not a model of SMBI to treat molecule transport properly without being confused with the models of GP and PI by either ignoring the convection process or including the complex ablation process.

Here, a practical fluid fuelling model of SMBI including convection is obtained by reduction of the Braginskii equations [15, 16] with source and sink terms due to collisional interactions. It includes transport equations of three particle species (molecules, atom and plasma), such as molecule density and radial momentum transport equations, atom density transport equation and plasma density, heat and momentum transport equations. Collision interactions between particles, such as dissociation, ionization, recombination, and charge-exchange effects, are included in the model. A boundary condition of molecule particle flux is applied locally in both poloidal and toroidal directions to model SMBI, which is more realistic than that of simply giving a source term in molecule density transport equation. According to HL-2A experiments, molecules are injected in the radial direction and transport mainly by convection during SMBI. Thus, we include a convection dominated molecule transport equation as well as a diffusion-dominated atom transport equation into a module, *trans-neut*, which is included into the BOUT++ edge plasma code. This model gives reasonable to describe transport dynamics during SMBI with classical fluid equations for the following reasons: (i) molecules are injected with an initial injection speed which is supersonic relative to its local thermal speed along radial direction, thus transport of molecules is dominated by convection rather than diffusion due to collisions; (ii) generation of atoms depends on where molecules are transported and the rate of dissociation by electrons, with atom/molecule collisions playing some role; (iii) inclusion of the *trans-neut* module in BOUT++ allows future 3D simulations, though the present modelling is 2D.

In somewhat more details, a number of transport models based on classical fluid equations have been used in previous studies. There have been several codes based classical fluid equations in toroidal tokamak geometry such as B2 [17], EPIC [14], UEDGE [13, 18], BOUT/BOUT++ [19–22] and TOKES [23]. The BOUT++ code is a framework for writing 2D and 3D fluid / plasma simulation in curvilinear geometry. Many applications have been developed in BOUT++ code, including boundary 3D turbulence simulations and edge-localized modes (ELMs) [24–30]. Besides turbulence studies on microscopic scales, BOUT++ has been recently developed to study the transport dynamics on macroscopic scales. The *trans-neut* module modifies the BOUT++ boundary plasma turbulence code to study the dynamics of neutrals transport and their interactions with plasma during fuelling by SMBI and it also provides a framework to study a multi-scale problem of mean profile evolution and ELM mitigation during the fuelling by SMBI by coupling with another BOUT++ module, elm-pb. Here mean profile evolution is on the plasma transport time scale ($\sim$tens of ms), while ELM events are on Alfven time scale ($\sim$tens of μs). Several simple 1D analytical tests of the code have been done against analytical solutions of Burger's equation, a diffusion–convection equation and a diffusion equation with/without spatio-temporal varying sources; show good agreement, as given in the appendix.

This paper reports simulations of neutrals penetration and plasma transport during fuelling by SMBI. Neutrals of both molecules and atoms and their interactions with the plasma are treated. Particle recycling at both the radial wall and divertor plates is included. To model SMBI, a specified local constant flux boundary condition in both radial and poloidal directions is applied. The physical model is described in section 2. The numerical implementation of boundary conditions is explained in section 3. Simulation results are illustrated in section 4. Finally, the principal results are summarized in section 5.

2. Physical model

In tokamak plasmas, there are many kinds of collision reactions between particles of molecules, atoms and plasmas during SMBI. It is difficult to include all of the reactions in a simple transport model of fuelling. For simplicity, only dominant reactions are necessary in modelling of particle transport, such as molecules dissociation, atoms ionization, ion–atom charge exchange, and electron–ion recombination. This simplifies the modelling of SMBI fuelling problems to four major particle species (i.e. hydrogen molecules, atoms, ions and electrons) and dominant reactions. According to different species of particles, the equations of the physical model can be divided into molecule, atom, and plasma transport. Transport of molecules and atoms are treated separately. A simple seven-field fluid model of SMBI, which couples plasma density, heat, and momentum transport equations together with neutrals density and momentum transport equations of both molecules and atoms, is obtained by reduction of the Braginskii equations with source and sink terms. This model captures some basic transport physics during SMBI such as perpendicular plasma

density and heat diffusion, parallel plasma density convection and heat conduction, energy interchange between electron and ion, parallel ion viscosity, atom diffusion, and molecule radial density convection. This simple model captures some basic features of transport during SMBI, but it needs future improvements, such as electric field and magnetic curvature drifted velocity, magnetic field shear, turbulent diffusion, momentum interchange between ion and atom etc. This work was conducted under the framework of the BOUT++ code [19]. Field-aligned coordinates (xyz) are applied in the simulation, which are related to the usual flux coordinates $(\psi\theta\zeta)$. It is important to note that the model is developed for 3D simulation in real tokamak magnetic geometry, although simulations done in this work are only in 2D of (xy) which are corresponding to $(\psi\theta)$ in flux coordinates. Some 3D simulations have also been done but will not be presented in this paper.

First, consider the plasma transport equations, including those for plasma density N_i, ion and electron temperatures (T_i, T_e) and parallel ion velocity $V_{\parallel\mathrm{i}}$. Plasma quasi-neutral condition (i.e. $N_\mathrm{i} = N_\mathrm{e}$) is applied. The equations are as follows:

$$\frac{\partial N_\mathrm{i}}{\partial t} + \nabla_\parallel\left(V_{\parallel\mathrm{i}}N_\mathrm{i}\right) - D^\mathrm{c}_{\perp\mathrm{i}}\nabla^2_\perp N_\mathrm{i} = S^\mathrm{p}_\mathrm{I} - S^\mathrm{p}_\mathrm{rec}, \tag{1}$$

$$\begin{aligned}\frac{\partial T_\mathrm{e}}{\partial t} &- \frac{2}{3N_\mathrm{i}}\nabla_\parallel\left(\kappa^\mathrm{c}_{\parallel\mathrm{e}}\nabla_\parallel T_\mathrm{e}\right) - \frac{2}{3}\chi^\mathrm{c}_{\perp\mathrm{e}}\nabla^2_\perp T_\mathrm{e}\\ &= \nu_\mathrm{rec}W_\mathrm{rec} - \nu_\mathrm{I}\left(T_\mathrm{e} + \frac{2}{3}W_\mathrm{I}\right)\\ &\quad -\frac{2}{3}\nu_\mathrm{diss}\left(W_\mathrm{diss} + W_\mathrm{bind}\right) - \frac{2m_\mathrm{e}}{M_\mathrm{i}}\frac{T_\mathrm{e}-T_\mathrm{i}}{\tau_\mathrm{e}},\end{aligned} \tag{2}$$

$$\begin{aligned}\frac{\partial T_\mathrm{i}}{\partial t} &+ V_{\parallel\mathrm{i}}\nabla_\parallel T_\mathrm{i} + \frac{2}{3}T_\mathrm{i}\nabla_\parallel V_{\parallel\mathrm{i}} - \frac{2}{3N_\mathrm{i}}\nabla_\parallel\left(\kappa^\mathrm{c}_{\parallel\mathrm{i}}\nabla_\parallel T_\mathrm{i}\right) - \frac{2}{3}\chi^\mathrm{c}_{\perp\mathrm{i}}\nabla^2_\perp T_\mathrm{i}\\ &= \left(\nu_\mathrm{rec} - \nu_\mathrm{I}\right)T_\mathrm{i} + \frac{2m_\mathrm{e}}{M_\mathrm{i}}\frac{T_\mathrm{e}-T_\mathrm{i}}{\tau_\mathrm{e}},\end{aligned} \tag{3}$$

$$\begin{aligned}\frac{\partial V_{\parallel\mathrm{i}}}{\partial t} &+ V_{\parallel\mathrm{i}}\nabla_\parallel V_{\parallel\mathrm{i}} - \frac{4}{3N_\mathrm{i}M_\mathrm{i}}\nabla_\parallel\left(\eta^0_\mathrm{i}\nabla_\parallel V_{\parallel\mathrm{i}}\right)\\ &= -\frac{\nabla_\parallel P}{N_\mathrm{i}M_\mathrm{i}} - \left(\nu_\mathrm{CX} + \nu_\mathrm{I}\right)V_{\parallel\mathrm{i}},\end{aligned} \tag{4}$$

where $D^\mathrm{c}_{\perp\mathrm{i}}$, $\chi^\mathrm{c}_{\perp\mathrm{e}}$, and $\chi^\mathrm{c}_{\perp\mathrm{i}}$ are perpendicular classical diffusion coefficients of density, electron temperature and ion temperature, respectively. $\kappa^\mathrm{c}_{\parallel\mathrm{e}}$ and $\kappa^\mathrm{c}_{\parallel\mathrm{i}}$ are parallel classical thermal conductivity coefficients. For simplicity, only the classical diffusivities/conductivities coefficients are considered here. η^0_i is parallel ion viscosity. S^p_I is the atom ionization source, while $S^\mathrm{p}_\mathrm{rec}$ is ion and electron recombination sink of plasma density (S^p representing particle source). ν_I, ν_rec, ν_diss and ν_CX are atom ionization rate, plasma recombination rate, molecule dissociation rate and ion-atom charge exchange rate, respectively. W_rec is the fraction of recombination energy re-absorbed by electron during recombination via some processes (i.e. three body recombination), while W_I and W_diss are electron energy lost per ionization and dissociation, and W_bind is the binding energy between the two hydrogen atoms in a molecule. Actually, those recombination terms are much smaller than the ionization terms due to the recombination rate is much lower than the ionization rate in hot plasma (i.e. $\nu_\mathrm{rec} \ll \nu_\mathrm{I}$) unless three-body recombination is included for $T_\mathrm{e} < 1\,\mathrm{eV}$. Thus, the influence of the recombination terms on transport dynamics can be ignored. $P = kN_\mathrm{i}(T_\mathrm{i} + T_\mathrm{e})$ is total plasma pressure, where k is Boltzmann's constant. Last terms on right hand side of equations (2) and (3) represent energy interchange between electrons and ions. τ_e is the electron–ion collision time. Since the electron parallel momentum transport is neglected in this simple model for simplicity, the electron heat convection term is also neglected. Even though there are not external heat source terms in the heat transport equations, there are ad hoc heat sources applied via flux-driven boundary conditions at core (as shown in section 3.1) to maintain the temperature profiles. In equation (4), ν_CX and ν_I appear with the same sign and serve as sink terms in the ion parallel velocity equation. It is because that there is no initial atom parallel velocity and the increase of total ion density in the ionization process leads to the decrease of the ion fluid velocity for momentum conservation.

In this simple model, only dominant atomic and molecular reactions are included, such as molecules dissociation, atoms ionization, ion-atom charge exchange, and electron-ion recombination. In molecule dissociation processes, an electron provides enough energy (W_diss) to break the binding between the two atoms in a molecule. In the atom ionization processes, atoms absorb energy (i.e. W_I) from electrons. In charge exchange processes, atoms and ions exchange their energies and there is no energy exchange if atoms and ions have the same energy (i.e. $T_\mathrm{a} = T_\mathrm{i}$). In recombination processes, electrons and ions lose energy (i.e. $\nu_\mathrm{rec}N_\mathrm{e}T_\mathrm{e}$ and $\nu_\mathrm{rec}N_\mathrm{i}T_\mathrm{i}$), atoms gain energy (i.e. $\nu_\mathrm{rec}T_\mathrm{a}$) which is assumed to be transferred back to ions due to high charge exchange rate. Besides, it assumes that there is a fraction of recombination energy re-absorbed by electron during recombination via some processes (i.e. three body recombination) (i.e. W_rec), but it can be ignored because the recombination rate is much lower than the other atomic and molecular reaction rates (i.e. ν_I, ν_diss and ν_CX) in a hot plasma ($\mathrm{T_e} \gg 1\,\mathrm{eV}$).

The second part of the model is the transport of atom density N_a. One of the simplest models for atom transport is based on atom diffusion caused by the strong charge exchange collision rate. Because the charge-exchange collision frequency is often the largest, the atom and ion temperature are typically assumed equal, i.e. $T_\mathrm{i} = T_\mathrm{a}$. The atom density transport equation is as following:

$$\frac{\partial N_\mathrm{a}}{\partial t} - \nabla_\parallel\left(D^\mathrm{c}_{\parallel\mathrm{a}}\nabla_\parallel N_\mathrm{a}\right) - D^\mathrm{c}_{\perp\mathrm{a}}\nabla^2_\perp N_\mathrm{a} = -S^\mathrm{p}_\mathrm{I} + S^\mathrm{p}_\mathrm{rec} + 2S^\mathrm{p}_\mathrm{diss}, \tag{5}$$

where, $D^\mathrm{c}_{\perp\mathrm{a}}$ and $D^\mathrm{c}_{\parallel\mathrm{a}}$ are perpendicular (to the magnetic field) and parallel atom diffusion coefficients, and $S^\mathrm{p}_\mathrm{diss}$ is the atom source due to molecule dissociation. Both parallel and perpendicular atom diffusion coefficients are simply calculated from atom force balance as

$$D^\mathrm{c}_{\perp\mathrm{a}} = D^\mathrm{c}_{\parallel\mathrm{a}} = D^\mathrm{c}_\mathrm{a} = T_\mathrm{a}/\left(M_\mathrm{a}\nu^\mathrm{a}_\mathrm{CX}\right). \tag{6}$$

In the atom diffusion process, the charge exchange dominates because of its larger rate coefficient than the recombination and dissociation rates. A more detailed atom model could be used that includes atom parallel momentum transport equation and the coupling of the parallel atom and ion velocities, but that this is not done in the present calculations.

The third part of the model is that for molecule transport, including molecule density N_m and radial velocity V_{xm} transport equations. The equations are as following:

$$\frac{\partial N_m}{\partial t} + \nabla_x (V_{xm} N_m) = -S^p_{diss}, \tag{7}$$

$$\frac{\partial V_{xm}}{\partial t} + V_{xm}\nabla_x V_{xm} = -\frac{\nabla_x P_m}{N_m M_m}, \tag{8}$$

where, $P_m = kN_mT_m$ is molecule pressure where molecule temperature T_m is the room temperature (i.e. 300 K). In the derivation of equation (8) from the molecule momentum transport equation, the collisions between molecules and electrons (i.e. dissociation) have been considered, while the collisions between molecules and atoms have been ignored due to their lower collision rate than the dissociation rate. The symbol ∇_x represents the radial component of the gradient. Molecule transport is mainly along the radial direction through the convection process due to its radial directed injection velocity during SMBI, while molecule transport is isotopic during GP. This model can also be used to simulate molecule transport during GP easily by switching off the local injection velocity at the wall boundary. A constant particle flux boundary condition localized in both poloidal and toroidal directions is applied at the outermost boundary flux surface with a constant molecule density and velocity, the details of which are shown below.

Definitions of quantities associated with the sources and rates due to particle collision reactions are as follows:

$$S^p_{rec} = N_e\nu_{rec}, \quad \nu_{rec} = N_i\langle\sigma_{rec}V_{th,e}\rangle,$$
$$S^p_I = N_e\nu_I = N_a\nu^a_I, \quad S^p_{CX} = N_i\nu_{CX} = N_a\nu^a_{CX},$$
$$S^p_{diss} = N_e\nu_{diss} = N_m\nu^m_{diss},$$
$$\nu_I = N_a\langle\sigma_I V_{th,e}\rangle, \quad \nu_{CX} = N_a\langle\sigma_{CX}V_{th,i}\rangle,$$
$$\nu_{diss} = N_m\langle\sigma_{diss}V_{th,e}\rangle,$$
$$\nu^a_I = N_e\langle\sigma_I V_{th,e}\rangle, \quad \nu^a_{CX} = N_i\langle\sigma_{CX}V_{th,i}\rangle,$$
$$\nu^m_{diss} = N_e\langle\sigma_{diss}V_{th,e}\rangle,$$

where $V_{th,e} = \sqrt{kT_e/M_e}$ and $V_{th,i} = \sqrt{kT_i/M_i}$ are electron and ion thermal velocity, respectively.

Rate coefficients in $\langle\ldots\rangle$ above are calculated by empirical formulas. $\langle\sigma_{rec}V_{th,e}\rangle$ is calculated by using the empirical formulas in [31], while the others are calculated as follows:

$$\langle\sigma_I V_{th,e}\rangle = 3\times10^{-8}(0.1T_e\text{eV})^2/[3+(0.1T_e\text{eV})^2]\,\text{cm}^3\,\text{s}^{-1}$$
$$\langle\sigma_{CX}V_{th,i}\rangle = 1.7\times10^{-8}+1.9\times10^{-8}$$
$$\times\frac{(1.5T_i\text{eV})^{1/3}-(15\,\text{eV})^{1/3}}{(150T_i\text{eV})^{1/3}-(15\,\text{eV})^{1/3}}\text{cm}^3\,\text{s}^{-1}$$
$$\langle\sigma_{diss}V_{th,e}\rangle = 3\times10^{-8}(0.1T_e\text{eV})^2/[3+(0.1T_e\text{eV})^2]\,\text{cm}^3\,\text{s}^{-1}.$$

Here, the rate coefficient of dissociation $\langle\sigma_{diss}V_{th,e}\rangle$ is assumed to be the same as the rate coefficient of ionization $\langle\sigma_I V_{th,e}\rangle$ because the molecules mainly dissociated in plasma edge where $T_{e,i} \approx 10$ eV and the rate coefficients of dissociation and ionization are about the same near 10 eV [32].

Definitions of other quantities associated with plasma physics are as follows:

$$\kappa^c_{\|e} = 3.2N_ekT_e\tau_e/m_e, \qquad \kappa^c_{\|i} = 3.9N_ikT_i\tau_i/M_i,$$
$$\eta^0_i = 0.96N_ikT_i\tau_i.$$

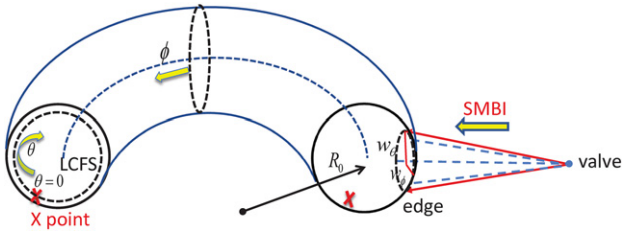

Figure 1. An SMBI configuration at HL-2A.

The physical quantities are normalized to characteristic parameters, such as $L_0 = 2.07$ m (the major radius of the HL-2A tokamak), $T_0 = 10$ eV (a reference plasma temperature), $V_0 = \sqrt{kT_0/M_i}$ (ion thermal velocity at T_0), $t_0 = L_0/V_0$ (a thermal transport time), $N_0 = 1\times10^{19}\,\text{m}^{-3}$ (a reference plasma density at core), $M_0 = M_p$ (the mass of the proton), and $B_0 = 1.96$ T (the maximum of magnetic field). In simulations, classical diffusion coefficients of plasma density and temperature are $D^c_{\perp i} = \chi^c_{\perp e} = \chi^c_{\perp i} = 1\,\text{m}^2\,\text{s}^{-1}$, energy associated with particle collisions are $W_{rec} = 4.5$ eV, $W_I = 20$ eV, $W_{diss} = 4.5$ eV, and $W_{bind} = 0.5$ eV. The coefficients of plasma parallel thermal conductivity ($\kappa^c_{\|e}$ and $\kappa^c_{\|i}$) are flux limited to prevent unphysical large values and recalculated as following:

$$\kappa^{cl}_{\|j} = \kappa^c_{\|j}\kappa^{fl}_{\|j}/\left(\kappa^c_{\|j}+\kappa^{fl}_{\|j}\right), \quad (j = \text{ei}), \tag{9}$$

where $\kappa^{fl}_{\|j} = V_{th,j}qL_0N_j$, $(j = \text{ei})$, are flux limited thermal conductivity coefficients, and q is a local magnetic safety factor. Here we take $q = q_{95}$ at position $\psi = 0.95$, i.e. at the 95% of the normalized flux surface.

Similarly, atom diffusion coefficients ($D^c_{\perp a}$ and $D^c_{\|a}$) are also flux limited and calculated as:

$$D^{cl}_{\perp a} = D^{cl}_{\|a} = D^c_{\|a}D^{fl}_{\|a}/\left(D^c_{\|a}+D^{fl}_{\|a}\right), \tag{10}$$

where $D^{fl}_{\|a} = V_{th,a}L_a$, $V_{th,a} = \sqrt{kT_a}/M_a$, and L_a is the gradient length at the steepest gradient region.

3. Numerical implementation of boundary conditions

In the HL-2A tokamak, SMBI can be injected from low field side (LFS) and high field side (HFS). In figure 1, an SMBI configuration on the LFS of HL-2A is shown to illustrate the general picture of SMBI fuelling. The real magnetic geometry, including the X-point, of the HL-2A tokamak is used. The cross-section of a tokamak geometry with X-point can be divided into three main regions [20]: the plasma core and edge region, the scrape-off-layer (SOL) region, the private flux and divertor plates region as shown in figure 2(*a*). In the BOUT++ code, the different regions of tokamak poloidal cross-section are shown in figure 2(*b*), which is useful for mapping the simulation results onto the tokamak poloidal cross-section. The poloidal angle is $\theta = 0$ at the X-point with positive values corresponding to a clockwise rotation in the poloidal direction. The divertor plates are located near poloidal angle $\theta = 0$ and poloidal angle $\theta = 2\pi$. The separatrix is located at the normalized magnetic flux $\psi = 1$. The main-chamber wall

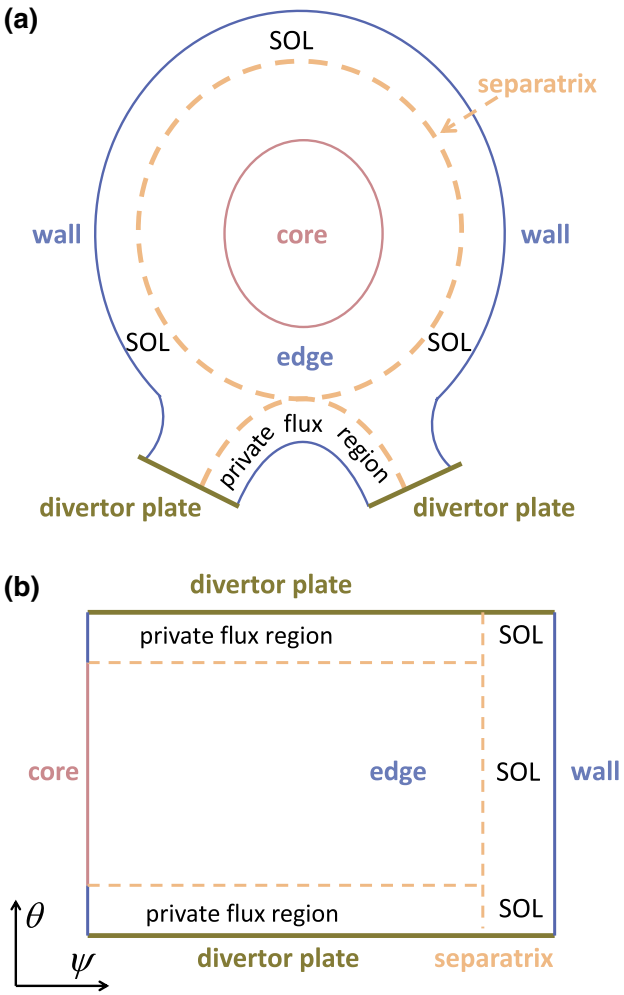

Figure 2. (*a*) Different regions of tokamak poloidal cross-section. (*b*) different regions of the tokamak poloidal cross-section in BOUT++ code.

is located at the outermost magnetic flux. Different boundary conditions are applied in the different regions.

Field-aligned coordinates (xyz) [19–21] are applied in the simulation with BOUT++ code, which are related to the usual flux coordinates ($\psi\theta\zeta$). In field aligned coordinates, x is the radial-like coordinate and x = const corresponds to a fixed flux surface; y is the poloidal-like coordinate and y = const corresponds to the direction along the magnetic field line; z is the toroidal-like coordinate in bi-normal direction. The coordinate Jacobian and metric coefficients are given for coordinate transformation in [21].

3.1. Radial (x) flux-driven boundary conditions

At the innermost boundary flux surface of core side, Neumann radial boundary conditions are set for all evolving quantities except for N_i, T_i and T_e, which are given fixed-gradient or flux-driven boundary conditions as follows:

$$\left.\frac{\partial N_\mathrm{i}}{\partial x}\right|_\mathrm{core} = -C_\mathrm{Ni}\frac{N_0}{L_0^2 B_0}, \tag{11}$$

$$\left.\frac{\partial T_\mathrm{e,i}}{\partial x}\right|_\mathrm{core} = -C_\mathrm{Te,i}\frac{T_0}{L_0^2 B_0}. \tag{12}$$

Where the coefficients $C_\mathrm{Ni} = 260$ and $C_\mathrm{Te,i} = 14000$ are input parameters and can be calculated from $C_\mathrm{Ni} = \Gamma_\mathrm{i}|_\mathrm{core} L_0^2 B_0 / D^\mathrm{c}_{\perp\mathrm{i}} \sqrt{g}^{11} N_0$ and $C_\mathrm{Te,i} = \mathrm{Q_{e,i}}|_\mathrm{core} L_0^2 B_0 / \frac{2}{3}\chi^\mathrm{c}_{\perp\mathrm{e,i}} N_\mathrm{i}|_\mathrm{core} \sqrt{g}^{11} T_0$ where $\Gamma_\mathrm{i}|_\mathrm{core}$ and $\mathrm{Q_{e,i}}|_\mathrm{core}$ are inflowing particle and heat fluxes at the innermost boundary flux surface on core side, respectively. The inflowing particle flux, $\Gamma_\mathrm{i}|_\mathrm{core} = -D^\mathrm{c}_{\perp\mathrm{i}} \left.\frac{\partial N_\mathrm{i}}{\partial R}\right|_\mathrm{core}$, is poloidally dependent and is about $9 N_0\,\mathrm{m\,s^{-1}}$. The inflowing heat flux, $\mathrm{Q_{e,i}}|_\mathrm{core} = -\frac{2}{3}\chi^\mathrm{c}_{\perp\mathrm{e,i}} N_\mathrm{i}|_\mathrm{core} \left.\frac{\partial T_\mathrm{e,i}}{\partial R}\right|_\mathrm{core}$, is also poloidally dependent and is about $10\,\mathrm{kW\,m^{-2}}$. The radial derivatives in flux coordinates can be converted into real-space coordinates by multiplying by $\sqrt{g}^{11} = RB_\theta$ as $\left.\frac{\partial f}{\partial R}\right|_\mathrm{core} = \sqrt{g}^{11}\left.\frac{\partial f}{\partial x}\right|_\mathrm{core}$. At the innermost boundary flux surface in the private flux region, N_i, T_i and T_e are given Dirichlet boundary conditions as $N_\mathrm{i}|_\mathrm{pf} = 0.1 N_0$ and $T_\mathrm{i}|_\mathrm{pf} = T_\mathrm{e}|_\mathrm{pf} = T_0$. These flux-driven boundary conditions at the core represent continuously inflowing particle and heat fluxes, or ad hoc effective local sources of particle and heat that are necessary to maintain the plasma profiles at steady state.

At the outermost flux surface in the SOL and private flux region, Neumann boundary conditions are also used for all evolving quantities except N_i, T_i, T_e and N_a. Of these variables, T_i and T_e used Dirichlet boundary conditions, the same as in the private flux region, while N_i and N_a are given particle recycling boundary conditions shown in the next section.

3.1.1. Wall particle recycling boundary conditions. Neutral atoms embedded in both the wall and the divertor plates can be recycled back into plasma and ionized there. Particle recycling is simulated with a simple model by introducing a recycling coefficient R_cyc, which gives the ratio between the outward plasma particle flux at a material surface and corresponding the inward atom neutral flux. Thus, the particle recycling boundary condition at the wall or the outermost boundary flux surface is:

$$\left.\frac{\partial \ln(N_\mathrm{i})}{\partial x}\right|_\mathrm{wall} = -\frac{1}{\sqrt{g}^{11} L^\mathrm{w}_\mathrm{ni}}, \tag{13}$$

$$\left.\frac{\partial N_\mathrm{a}}{\partial x}\right|_\mathrm{wall} = \frac{\Gamma^\mathrm{w}_\mathrm{a}}{\sqrt{g}^{11} D^\mathrm{c}_{\perp\mathrm{a}}}, \tag{14}$$

where the plasma density gradient length at the wall $L^\mathrm{w}_\mathrm{ni} = 5\,\mathrm{cm}$ is an input parameter, recycling atom particle flux at the wall $\Gamma^\mathrm{w}_\mathrm{a} = R_\mathrm{cyc}\Gamma^\mathrm{w}_\mathrm{i} = R_\mathrm{cyc} D^\mathrm{c}_{\perp\mathrm{i}} N_\mathrm{i} / L^\mathrm{w}_\mathrm{ni}$. Particle recycling at the divertor plates is described in section 3.2.2. In simulations, the recycling coefficient $R_\mathrm{cyc} = 1$ is used, which means all the outgoing plasma fluxes have been recycled via the inflowing atom fluxes at both the wall and the divertor plates.

3.1.2. SMBI localized boundary conditions. In experiments, SMBI is injected with a constant inflowing molecule particle flux localized in both poloidal (y) and toroidal (z) directions at the far SOL boundary of the tokamak. To model this, a constant particle flux boundary condition is set for both molecule density and radial velocity at the outermost boundary flux surface of simulation domain within a local (yz) region during SMBI. This local constant flux boundary condition is more realistic for modelling SMBI instead of simply adding a source term in molecule density transport equation. In the 2D (xy) simulation, it is assumed that the SMBI device is

toroidal symmetrically injected in the whole range of toroidal simulation domain and localized within a poloidal range $\theta_0 \leqslant \theta \leqslant \theta_1$ with a constant density $N_{\mathrm{m}0}$ and a radial velocity $V_{x\mathrm{m}0}$. To avoid numerical instability due to sharp gradient in poloidal direction, an exponential profile of particle flux is used. Therefore, the local constant flux boundary condition is modified as follows:

$$N_{\mathrm{m}}|_{\mathrm{edge}} = N_{\mathrm{m}0}\exp\left(-\left(\theta-\theta_{1/2}\right)^2/\left(w_\theta/a\right)^2\right) \quad (\theta_0 \leqslant \theta \leqslant \theta_1)\,, \tag{15}$$

$$V_{x\mathrm{m}}|_{\mathrm{edge}} = V_{x\mathrm{m}0}\exp\left(-\left(\theta-\theta_{1/2}\right)^2/\left(w_\theta/a\right)^2\right) \quad (\theta_0 \leqslant \theta \leqslant \theta_1)\,, \tag{16}$$

where the fuelling source centre $\theta_{1/2} = (\theta_0+\theta_1)/2$, w_θ is a poloidal width of SMBI at the outermost boundary flux surface, and a is minor radius. In 3D (xyz) simulations, a similar localized SMBI will be applied in toroidal direction.

The experimental set-up of the SMBI system in the HL-2A tokamak is shown in [3]. The SMBI lies on the equatorial plane and is aimed perpendicular to the magnetic axis of HL-2A. The diameter of the valve for producing the supersonic molecule beam is about 0.2 mm. The pressure of the beam is in the range 0.25–3.0 Mpa, its temperature is about 300 K (the room temperature), and its density at the valve is in the range 6.2×10^{25}–$7.4\times10^{26}\,\mathrm{m}^{-3}$. Because the distance between the valve and the plasma edge is as long as 1.28 m, the molecule density decreases as the cross-section of the beam increases. The molecule density at plasma edge is simply calculated as $N_{\mathrm{m}0} = N_{\mathrm{m}}^{\mathrm{v}} r_{\mathrm{val}}^2/r_{\mathrm{edge}}^2$, where $r_{\mathrm{val}} = 0.1$ mm and $r_{\mathrm{edge}} \approx 16$ cm are the radii of the beam cross-sections at the valve and the plasma edge, respectively. A molecule injection speed in a range of 500–1200 $\mathrm{m\,s}^{-1}$ is assumed to be same at both the valve and the plasma edge. In simulations, we choose $N_{\mathrm{m}0} = N_0 = 1\times10^{19}\,\mathrm{m}^{-3}$, and $V_{x\mathrm{m}0} = -1000\,\mathrm{m\,s}^{-1}$ according the experiment parameters of SMBI in HL-2A.

3.2. Poloidal (y) boundary conditions

For all the evolving quantities, pseudo-periodic boundary conditions are applied in y in 'Edge' (the outer part of the closed flux region inside the separatrix). At the divertor plates, sheath boundary conditions are applied for plasma N_{i}, T_{i}, T_{e} and V_{i}, and a particle recycling boundary condition is applied for atom density N_{a}. For simplicity, we assume here that the poloidal magnetic field is normal to the divertor plates.

3.2.1. Sheath boundary conditions. At the divertor plates, an electrostatic sheath is formed to reflect all but high-energy electrons so that the ion and electron particle fluxes into the divertor plates are equal; thus it also influences the energy fluxes leaving the plasma. The outgoing sheath particle flux is $\Gamma_{\mathrm{i}}^{\mathrm{d}} \equiv N_{\mathrm{i}}c_{\mathrm{se}}$ where $c_{\mathrm{se}} = \sqrt{k(T_{\mathrm{i}}+T_{\mathrm{e}})}/M_{\mathrm{i}}$ and the total transmission heat fluxes are $\mathrm{Q}_{\mathrm{e,i}}^{\mathrm{d}} \equiv \gamma_{\mathrm{e,i}}kT_{\mathrm{e,i}}\Gamma_{\mathrm{i}}^{\mathrm{d}}$ where $\gamma_{\mathrm{e}} \approx 7$ and $\gamma_{\mathrm{i}} \approx 2.5$ are electron and ion sheath heat transmission factors, respectively. Therefore, the sheath boundary conditions are the following:

$$V_{\parallel\mathrm{i}}|_{\theta=0} = -\,c_{\mathrm{se}}|_{\theta=0}\,;\; V_{\parallel\mathrm{i}}|_{\theta=2\pi} = c_{\mathrm{se}}|_{\theta=2\pi}\,, \tag{17}$$

$$\nabla_\parallel N_{\mathrm{i}}|_{\theta=0} = 0;\; \nabla_\parallel N_{\mathrm{i}}|_{\theta=2\pi} = 0, \tag{18}$$

$$\nabla_\parallel T_{\mathrm{e,i}}|_{\theta=0} = \mathrm{Q}_{\mathrm{e,i}}^{\mathrm{d}}/\left(k\kappa_{\parallel\mathrm{e,i}}^{\mathrm{c}}\right)|_{\theta=0}\,;\; \nabla_\parallel T_{\mathrm{e,i}}|_{\theta=2\pi} = -\,\mathrm{Q}_{\mathrm{e,i}}^{\mathrm{d}}/\left(k\kappa_{\parallel\mathrm{e,i}}^{\mathrm{c}}\right)|_{\theta=2\pi}\,. \tag{19}$$

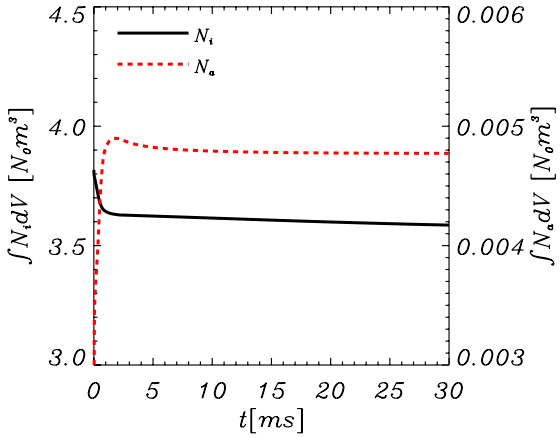

Figure 3. Time evolution of total particles: $\int N_{\mathrm{i}}\mathrm{d}V$ (black solid curve) and $\int N_{\mathrm{a}}\mathrm{d}V$ (red dashed curve) integral whole volume of tokamak, and saturation state is reached.

The divertor plates are located near $\theta = 0$ and $\theta = 2\pi$. The positive signs in equations above are along the poloidal direction. Both positive and negative values of the sheath boundary conditions at $\theta = 0$ or $\theta = 2\pi$ all depend on the directions of local outgoing particle and heat fluxes which are varying in both time and space.

3.2.2. Divertor particle recycling boundary condition. According to sheath boundary conditions of plasma density and ion velocity, the plasma particle flux onto the divertor plates is $\Gamma_{\mathrm{i}}^{\mathrm{d}} \equiv N_{\mathrm{i}}c_{\mathrm{se}}$. Recycling atom particle flux from divertor plates is simply $\Gamma_{\mathrm{a}}^{\mathrm{d}} \equiv R_{\mathrm{cyc}}\Gamma_{\mathrm{i}}^{\mathrm{d}}$ as used at the wall.

$$\nabla_\parallel N_{\mathrm{a}}|_{\theta=0} = -\,\Gamma_{\mathrm{a}}^{\mathrm{d}}/D_{\parallel\mathrm{a}}^{\mathrm{c}}|_{\theta=0}\,;\; \nabla_\parallel N_{\mathrm{a}}|_{\theta=2\pi} = \Gamma_{\mathrm{a}}^{\mathrm{d}}/D_{\parallel\mathrm{a}}^{\mathrm{c}}|_{\theta=2\pi}\,. \tag{20}$$

4. Simulation results

4.1. Steady states with and without particle recycling before SMBI

Initial profiles of plasma density and temperatures with linear variations in x are specified according to the flux-driven boundary conditions. With particle recycling, a steady state of the system is reached. As shown in figure 3, the total particles of plasma and atom are conserved after it reaches the steady state, which are calculated by integrating plasma and atom densities over the whole volume of tokamak (i.e. $\int N_{\mathrm{i}}\mathrm{d}V = \int N_{\mathrm{i}}J\mathrm{d}\psi\mathrm{d}\theta\mathrm{d}\zeta$ and $\int N_{\mathrm{a}}\mathrm{d}V = \int N_{\mathrm{a}}J\mathrm{d}\psi\mathrm{d}\theta\mathrm{d}\zeta$). Total plasma density decreases at first and then saturates, while total atom density increases and saturates. The initial decrease of the plasma density is due to plasma outflows in the private flux region and SOL region, while the initial increase in the total atom density is due to atom inflow from recycling at the divertor plates and the wall. There are a slight variations (<1% within 30 ms) of the total plasma and atom number at the steady state. By considering it is plasma fuelling study of SMBI (much larger density variations within 1 ms), those small variations are negligible. Plasma density and atom density profiles at steady state are shown in figures 4(a) and (b), respectively. To map these surface plots onto 2D poloidal cross-section, refer back to figure 2(b) for more details. In figure 4(a), plasma density is plotted at steady

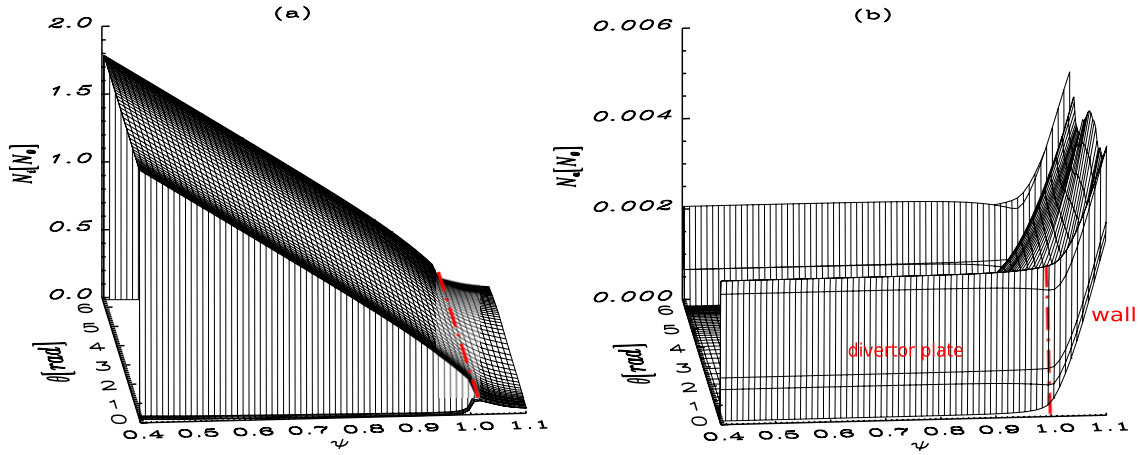

Figure 4. (*a*) $N_{\rm i}$ and (*b*) $N_{\rm a}$ at steady state with particle recycling, red dash dotted lines representing the separatrix.

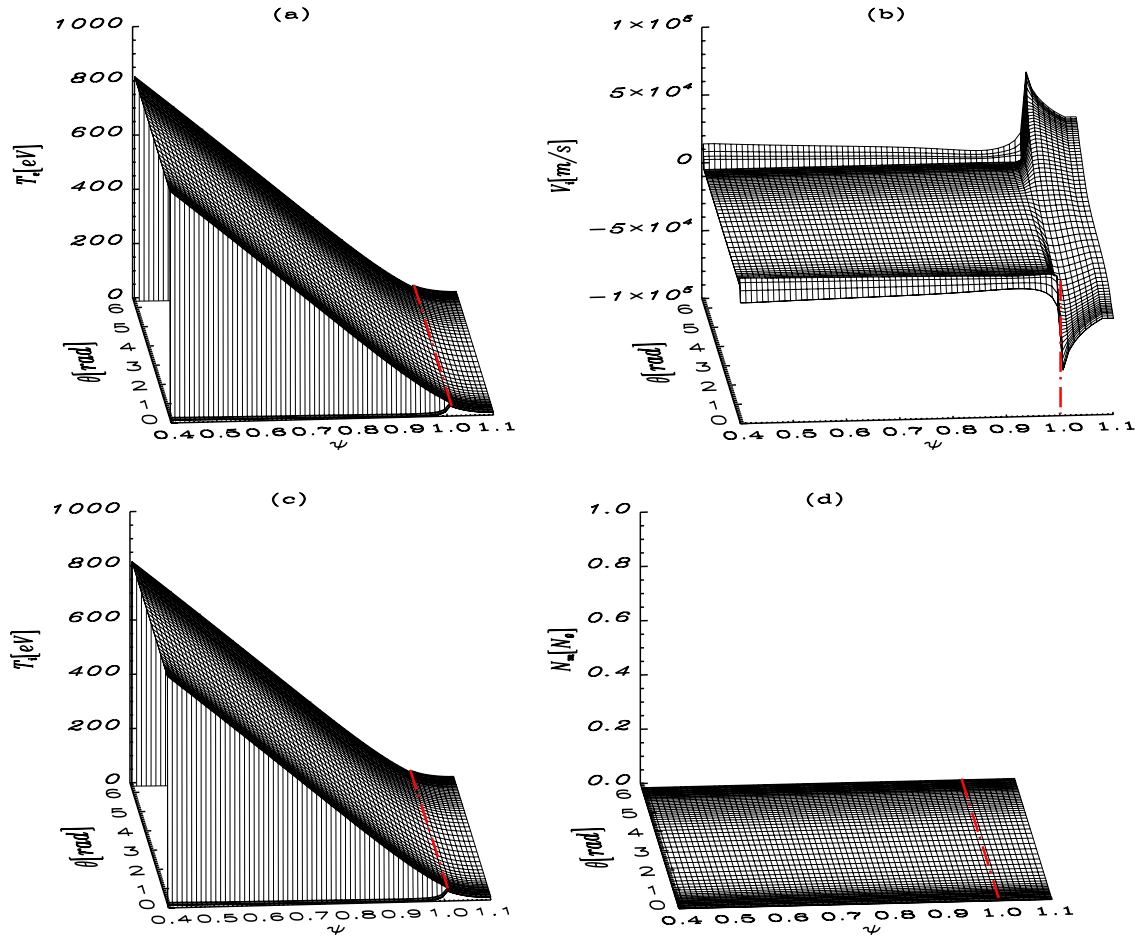

Figure 5. Other evolving quantities of (*a*) $T_{\rm e}$, (*b*) $V_{\rm i}$, (*c*) $T_{\rm i}$ and (*d*) $N_{\rm m}$ at steady state with particle recycling, red dash dotted lines representing the separatrix.

state determined by the boundary conditions of flux-driven boundary condition, particle recycling boundary condition, and sheath boundary condition. Inside of the separatrix, plasma density is nearly linearly proportional to radius due to the flux-driven boundary condition of plasma density. Outside the separatrix, the decrease of plasma density is due to the particle flux outgoing towards both the wall and the divertor plates. There is a very low plasma density in the private flux regions (i.e. $0.4 < \psi < 1.1$ and $0\,{\rm rad} \leqslant \theta \leqslant 0.39\,{\rm rad}$ or $5.88\,{\rm rad} \leqslant \theta \leqslant 6.28\,{\rm rad}$) due to the private flux boundary condition. In figure 4(*b*), atom density is plotted at steady state and particle recycling at both the wall and the divertor plates is clearly evident. The steady state of atom density with particle recycling is determined by the particle recycling boundary condition (i.e. atom source) and its local ionization rate (i.e. atom sink).

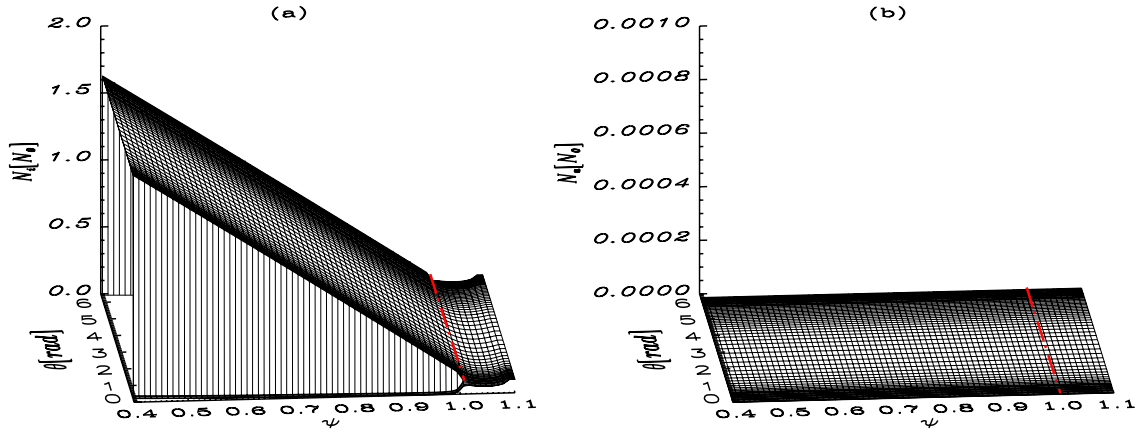

Figure 6. (a) N_i and (b) N_a at steady state without particle recycling, red dash dotted lines representing the separatrix.

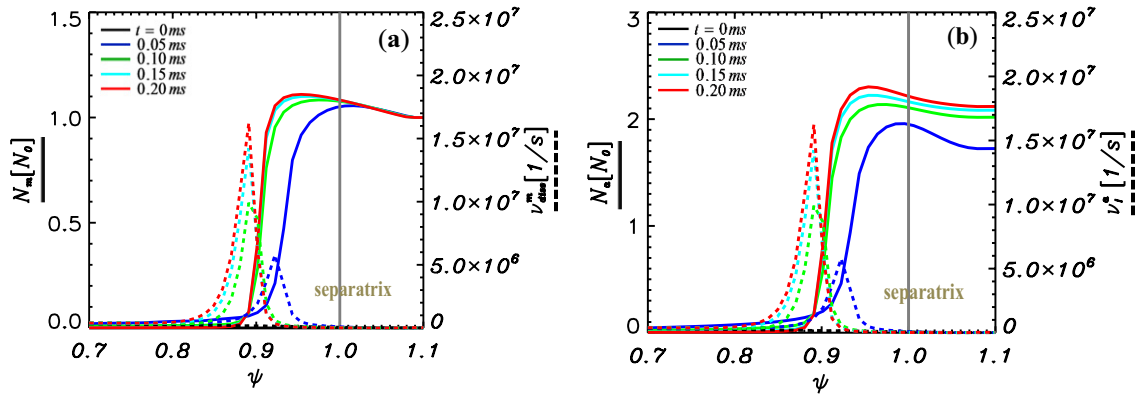

Figure 7. Time evolution of radial profiles: (a) N_m (solid curve) and its dissociation rate ν^m_{diss} (dashed curve), (b) N_a (solid curve) and its ionization rate ν^a_i (dashed curve) plotted at outer mid-plane during inward propagation of SMBI. Neutrals propagate inwards and into the separatrix for about 4 cm, their front propagating speeds decrease, and the front gradients increase due to the increase of dissociation rate and ionization rate.

State profiles of T_e, T_i, V_i and N_m are shown in figure 5. Same as plasma density, the steady states of plasma temperatures (figures 5(a) and (c)) are determined altogether by the boundary conditions of flux-driven boundary condition, fixing to a constant value at the outermost boundary flux surface and sheath boundary condition in the parallel direction. In figure 5(b), there are both negative V_i at $\theta = 0$ and positive V_i at $\theta = 2\pi$ which is due to sheath boundary condition of plasma ion velocity and they all represent outgoing fluxes of plasma density and heat towards the divertor plates. There is no initial molecule density before SMBI (figure 5(d)). After the system reaches its steady state, SMBI is turned on (section 4.2) to study the transport dynamics of neutrals and plasma during the fuelling process.

Without particle recycling (i.e. $R_{cyc} = 0$ in the divertor plate and wall boundary conditions), the steady states of T_e, T_i, V_i and N_m are about all the same as those with particle recycling because particle recycling mainly affects the plasma density profile (figure 6(a)) and especially the atom density profile (figure 6(b)). There will be no any atom density without particle recycling. Plasma density is fixed to $0.1N_0$ at the outermost boundary flux surface without particle recycling, while it is fixed to a constant gradient length at the outermost boundary flux surface with particle recycling. Because there is more outgoing particle flux without particle recycling than with particle recycling at the outermost boundary flux surface, ion density at $\psi = 0.4$ without particle recycling (figure 6(a)) is lower than that with particle recycling (figure 4(a)).

4.2. Transport dynamics during SMBI

Transport dynamics with SMBI is studied after the system reaches its steady state which is set as $t = 0$ ms. In simulations, the duration of SMBI is about 1 ms with a constant molecule density $N_{m0} = N_0$ and an inward constant radial velocity $V_{xm0} = -1000\,\mathrm{m\,s^{-1}}$. Transport dynamics in both radial and poloidal directions are going to be studied during SMBI.

Firstly, it is going to study the dynamics of neutrals and plasma transport in the radial direction during SMBI. Inward propagation of neutrals has been observed during SMBI as shown in figure 7. There are no molecules at $t = 0$ ms and there is a small recycled atom density, about two orders lower than the atom density during SMBI. In figure 7(a), molecules propagate inwards across the separatrix. In figure 7(b), atom density is about twice of the molecule density at all times (i.e. one molecule being dissociated into two atoms) and the increase of atom density at edge is due to the diffusion of atoms from the inside of the separatrix. Because the time interval between different two solid curves are the same in figure 7, the radial distance between two curves is decreasing, which

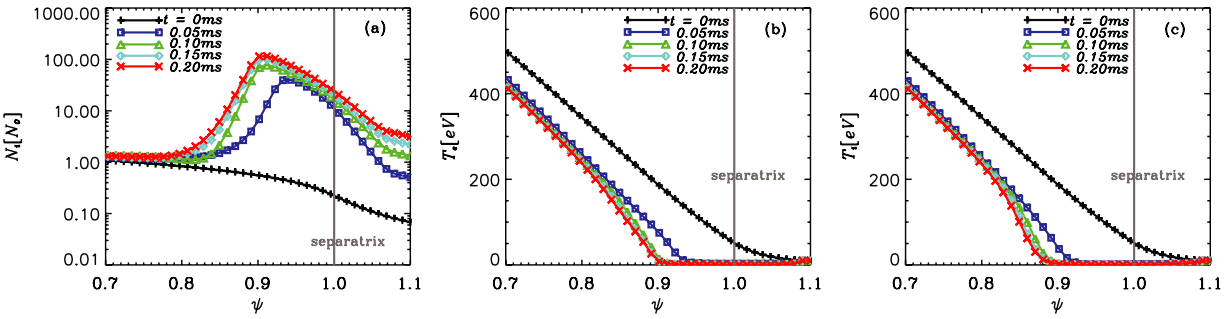

Figure 8. Time evolution of radial profiles: (*a*) N_i, (*b*) T_e and (*c*) T_i, plotted at outer mid-plane during inward propagation of neutrals. Local plasma density increase and temperature decrease are observed.

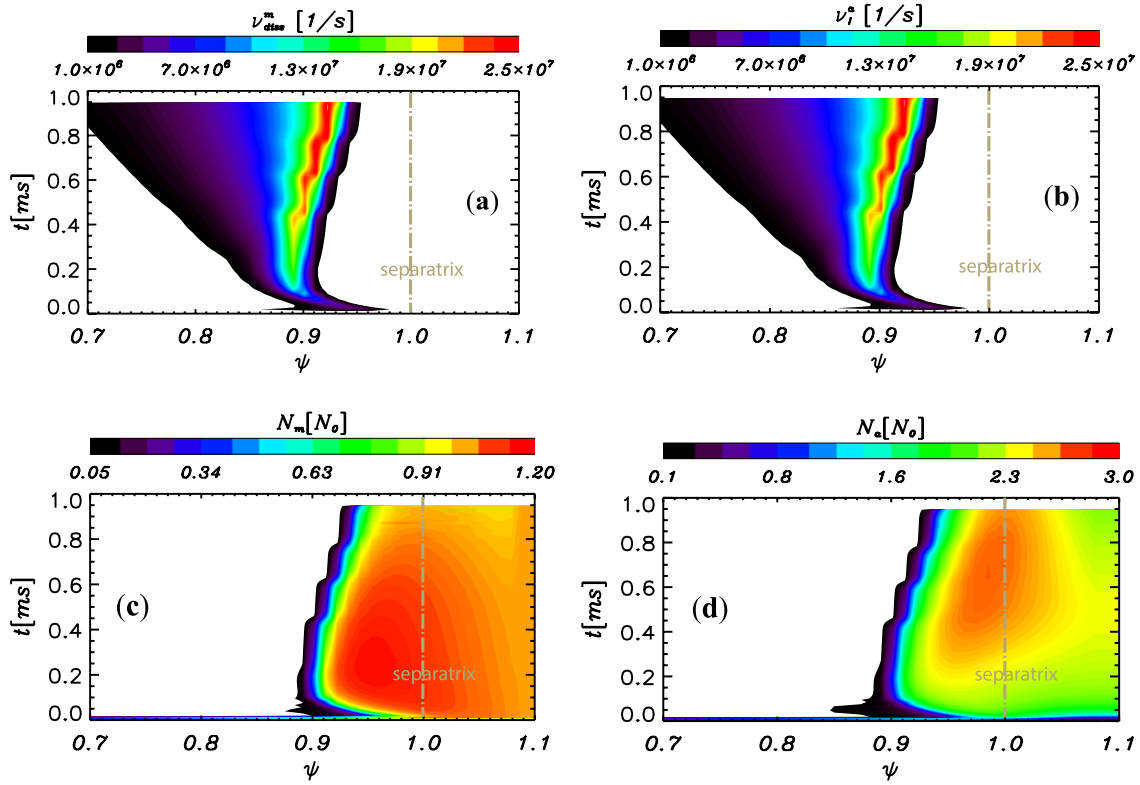

Figure 9. Time and spatial evolutions: (*a*) ν^{m}_{diss}, (*b*) ν^{a}_{I}, (*c*) N_m and (*d*) N_a, plotted at outer mid-plane during SMBI. It is found that neutral fronts first propagate inwards continuously and then move outwards step by step due to the increase of dissociation and ionization rates.

means the propagation speed of molecules becomes smaller as it propagates deeper into the plasma because of the increased molecule dissociation rate. The molecule density at the leading edge of the beam is larger than that at source boundary and this difference increases as the beam propagates into the plasma due to the decrease of molecule propagation speed. Once the total molecule dissociation rate $R^{diss}_m = \int N_m \nu^m_{diss} dV$ increases at the beam front to the beam's injection rate $R^{in}_m = (N_m\ V_{xm} S_m)|_{edge}$, the molecule beam front stops moving inward. The penetration depth of molecule is about 4 cm inside of the separatrix. This depth depends on both the local plasma conditions (i.e. N_i, $T_{e,i}$) and the molecule injection rate. It penetrates deeper during SMBI in L-mode, which has lower plasma density and temperatures resulting in a low dissociation rate. The penetration depth also increases with the increase of molecule beam injection velocity. The same is true for the subsequent atom propagation because its ionization rate increases during the inward propagation (figure 7(*b*)). During inward propagation of neutrals, plasma density is locally increasing and temperatures are locally decreasing along the beam path as shown in figure 8. Plasma density increases dramatically with time in the region, especially near beam front (figure 8(*a*)), due to the ionization of atoms. Electron temperature decreases due to electron energy loss in the processes of dissociation and ionization, while ion temperature decreases due to the increase of ion density and energy interchange between electrons and ions.

During the injection of SMBI, plasma density will keep increasing which leads to the increase of the dissociation and ionization rates of neutrals (figures 9(*a*)–(*b*)). Once the total molecule dissociation rate becomes larger than its injection rate, the molecule propagation front will begin to move outwards step by step as shown in figure 9(*c*). The same is true for the atom propagation front (figure 9(*d*)). Thus, the initial inward propagation of the neutral density is arrested and changes direction at the later stages of sustained SBMI. The

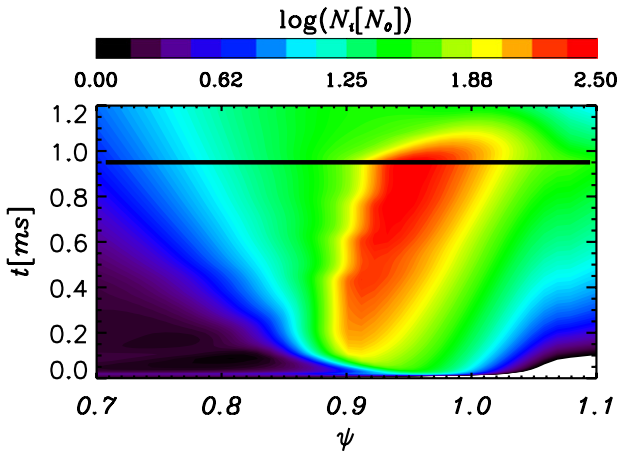

Figure 10. Time and space evolution of N_i, while the black dashed line represents the turn-off of SMBI. It is found that the peak of ion density is moving outwards step by step during SMBI and continuously after SMBI.

reason for the outward movement is still not quite clear yet, but it is clearly seen in the result shown in figure 10. We believe that the outward step by step propagation is due to the competition between the total molecule dissociation rate and the injection rate of the molecules, while the threshold of outward propagation at each step should be determined by the constant injection rate of SMBI. The physical picture of these events is: (1) plasma density peak keeps increasing until that total molecule dissociation rate becomes larger than the molecule injection rate; (2) plasma density peak then moves outwards and decreases, which leads to the total molecule dissociation rate becoming smaller than its injection rate; (3) the plasma density peak increases, again moving the peak outward.

Second, dynamics of plasma particle and heat transport in the poloidal direction is also studied during SMBI. As shown in figure 11, the poloidal profiles of plasma density and temperatures are uniform in parallel direction at steady state before SMBI. Later with SMBI, the plasma density peaks poloidally in the region of SMBI (figure 11(a)), while both electron and ion temperatures decrease in the region of SMBI, which then decreases the nearby temperatures due to parallel heat conduction (figures 11(b) and (c)). The discontinuity of the poloidal profiles plotted outside of the separatrix is due to the sheath boundary condition applied at the divertor plates, while a periodic boundary condition is applied inside the separatrix (details in section 3.2). Parallel pressure gradient drives both positive and negative parallel ion velocities near the region of SMBI (figure 12(a)). These positive and negative ion velocities spread the peaked plasma density in both positive and negative poloidal directions, as shown in the 1D poloidal plots shown in figure 11(a). Because electron parallel thermal conductivity (figure 12(b)) is about two orders larger than ion parallel thermal conductivity (figure 12(c)), parallel electron (conductive) heat transport is much faster than ion heat transport. Ion parallel heat transport has comparable contributions from both conduction and convection. The difference between the electron and ion thermal transport can be seen in figure 11(b) (conduction only) and figure 11(c) (both conduction and convection) that the width of the hole does not change in figure 11(b) but it spreads out in figure 11(c). This is because the parallel convection dominates the parallel ion heat transport rather than the conduction-dominated electron case as shown in figure 13. Also, the localized heat loss from dissociation and ionization comes directly from the electron channel.

As shown in figures 14–16, SMBI acting as both a particle source and a heat sink will lead to locally peaked plasma density and reduced plasma temperatures. Before SMBI, both the plasma density and temperatures are uniform in parallel direction at steady state. Later, SMBI generates a locally peaked plasma density blob and temperature holes. Due to poloidal convection, a plasma density blob (figure 14) and an ion temperature hole (figure 15) spread both upwards and downwards in the cross-section of tokamak during SMBI. Because electron heat convection is not included in this simple model, electron heat transport depends on parallel thermal conductivity only. Without the electron convection terms, electron temperature holes become deeper and deeper but remain at the same location of SMBI during continuous injection (figure 16). Both the upward and downward blob propagation of plasma density have the same poloidal speed (figure 12(a)) away from the SMBI location. Due to the symmetry of particle poloidal propagation away from SMBI location, both upward and downward propagating particle fluxes reinforce one another and form a plasma density peak at the inner mid-plane opposite the peak at outer mid-plane (figures 14(c)–(d)). With the increase of the inner plasma density peak, the two plasma density peaks are merging together with one and the other (figure 14(e)). Propagation of ion temperature hole toward the divertor plate is also observed (figures 15(b)–(e)). The duration of SMBI is 0.95 ms. After the cessation of the SBMI, it takes about 2.5 ms for the system to recover back to the poloidally uniform plasma density (figure 14(f)), ion temperature (figure 15(f)) and electron temperature (figure 16(f)), but it is still evolving in radial direction towards the final steady state determined by the boundary conditions.

4.3. Relaxation of profiles after SMBI

After SMBI, the remaining molecules and atoms will be quickly dissociated and ionized. It takes about 2.5 ms for the system to become poloidally uniform first via poloidal transport of plasma density and heat. Mean profiles are also relaxing in the radial direction after SMBI but they need a long time to reach the steady state, about 60 ms (figure 17). Overall plasma density and pressure increase (figures 17(a) and (b)) while both electron and ion temperatures decrease (Figures 17(c) and (d)) after SMBI. A steeper pressure gradient region is observed near the separatrix at $t = 3.5$ ms due to the increase of plasma density in that region. The radially localized peaked plasma density spreads out which leads to the increase of plasma density and pressure in the core-edge region at $t = 7.5$ ms. Because the inflowing particle flux at the innermost boundary flux surface on the core side is smaller than the outgoing particle flux through both the wall and divertor plates, plasma density decreases globally, returning to the initial steady state before SMBI (figure 17(a)). Thus, plasma pressure profile also decreases, relaxing back to its

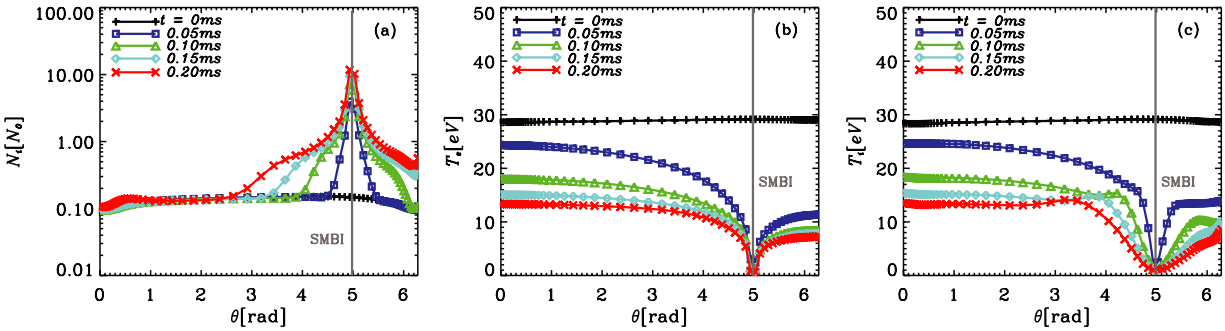

Figure 11. Time evolution of poloidal profiles: (*a*) N_i, (*b*) T_e and (*c*) T_i, plotted at normalized $\psi = 1.03$ during SMBI. Poloidal plasma density profile is locally peaked while plasma temperatures are dropped at SMBI location. Both upward and downward poloidal propagation of plasma density and temperature are observed.

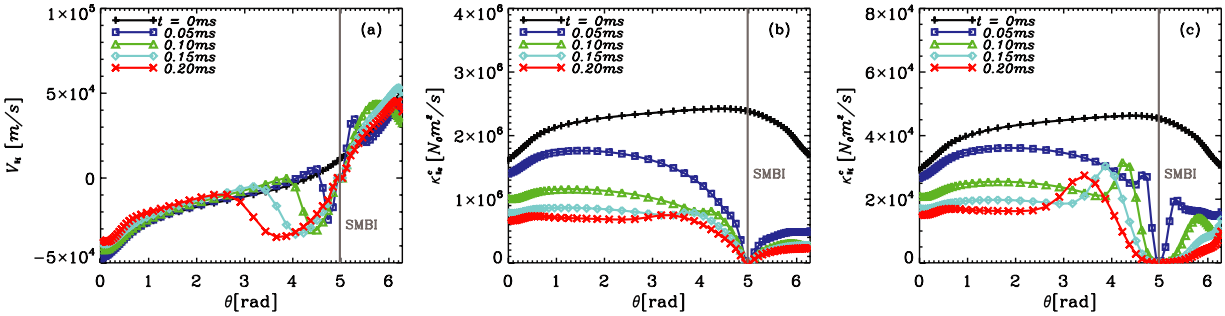

Figure 12. Time evolution of poloidal profiles: (*a*) $V_{\|\mathrm{i}}$, (*b*) electron thermal conductivity $\kappa_{\|\mathrm{e}}$ and (*c*) ion thermal conductivity $\kappa_{\|\mathrm{i}}$. Both positive and negative ion velocities are driven by SMBI due to parallel pressure gradient. Plasma thermal conductivities are dropped in SMBI location and also propagate both upwards and downwards in parallel direction.

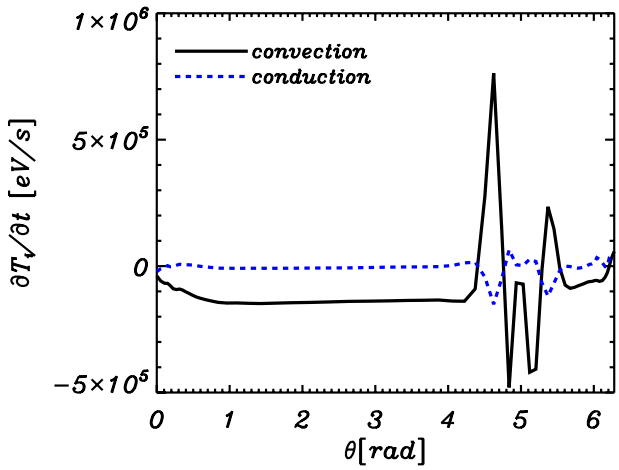

Figure 13. Time derivative of ion temperature due to convection term of $-V_{\|\mathrm{i}}\nabla_\| T_\mathrm{i} - \frac{2}{3}T_\mathrm{i}\nabla_\| V_{\|\mathrm{i}}$ (black curve) and conduction term of $(2/3N_\mathrm{i})\nabla_\|\left(\kappa^\mathrm{c}_{\|\mathrm{i}}\nabla_\| T_\mathrm{i}\right)$ (blue dashed curve) at $t = 0.05$ ms during SMBI, where parallel convection term dominates in ion heat transport.

initial state (figure 17(*d*)). Meanwhile, both electron and ion temperatures are increasing and finally return to the initial profiles on a time scale of 60 ms. All the steady states of plasma density, pressure and temperatures are determined by the boundary conditions only. It is not adiabatic during the relaxation process after SMBI because there are continuously inflow of heat via the flux-driven boundary conditions at the core and outflow of heat fluxes at material interfaces. Because the heat relaxation times of the temperature profiles back to their steady states are less than the particle relaxation time of density profile back to its steady state, there is still large variation of the density profile while the temperature profiles are almost constant. These simulations present the complete transport dynamics for the plasma and neutral components during the three distinct phases: evolution to steady state before SMBI, transport during SMBI, and relaxation back to the initial steady state after SMBI.

5. Summary and conclusions

A plasma fuelling model of SMBI including density, temperature and momentum transport equations for molecules, atoms, and plasma is developed. Collisional interactions between molecules, atoms, and plasma are included, such as molecule dissociation, atom ionization, atom charge exchange with ion, and electron and ion recombination. A new module for SMBI, *trans-neut*, is developed and added to the BOUT++ code for real tokamak geometry with an X-point. SMBI is modelled with a constant particle flux boundary condition localized in both poloidal and toroidal directions at the outermost boundary flux surface by giving a constant molecule density and a constant injection speed rather than specifying a source term in molecule density transport equation. Flux-driven boundary conditions and sheath boundary conditions are applied for plasma density and temperatures. Particle recycling at both wall and divertor plates are also included. Transport dynamics of plasma and neutrals are simulated for a complete range of discharge times, including steady state

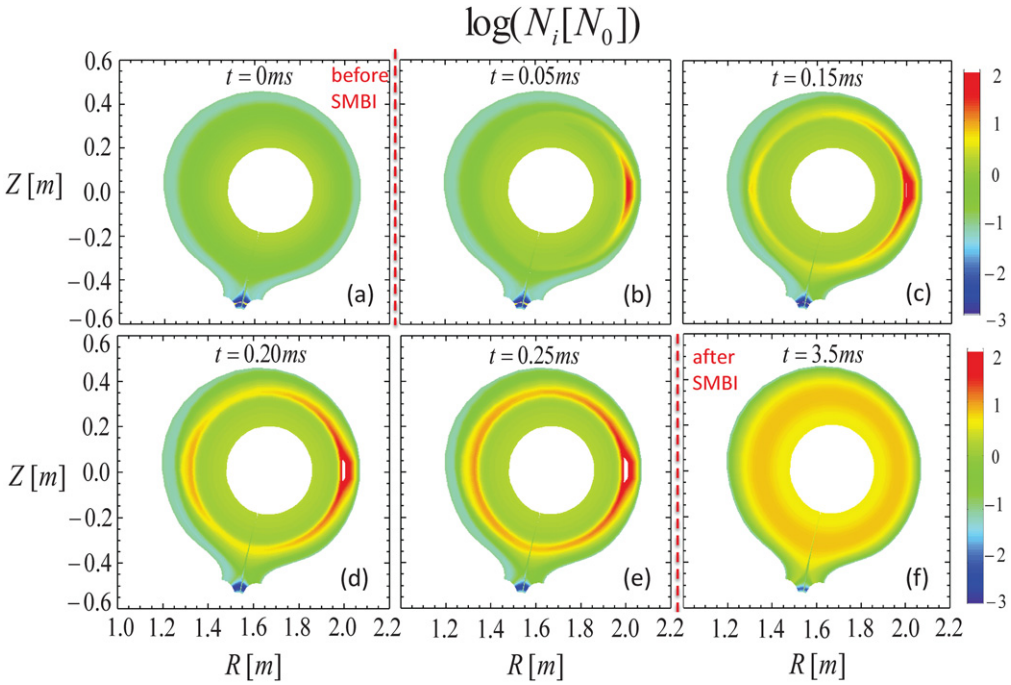

Figure 14. Poloidal blob propagation of plasma density due to poloidal convection during a duration of 0.95 ms SMBI plotted in the cross-section of tokamak at different times. Plasma density is poloidally uniform before SMBI and also about 2.5 ms after SMBI.

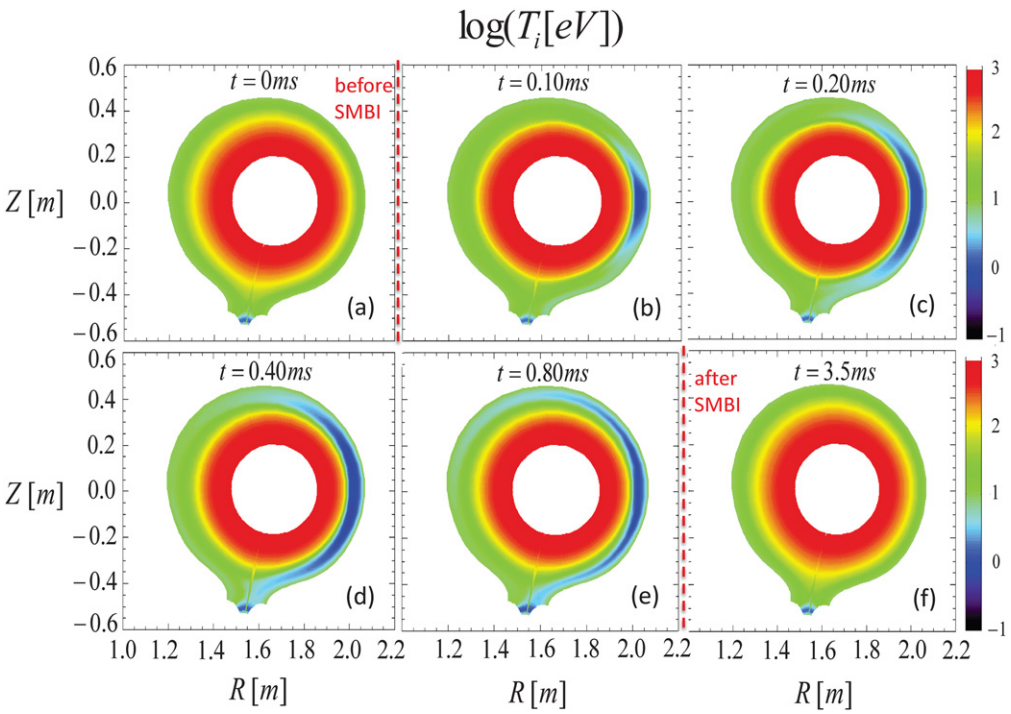

Figure 15. Poloidal hole propagation of ion temperature sink due to poloidal convection during a duration of 0.95 ms SMBI plotted in the cross-section of tokamak at different times. Plasma ion temperature is poloidally uniform before SMBI and also about 2.5 ms after SMBI.

before SMBI, transport during SMBI, and relaxation back to the initial steady state after SMBI. Principal results are summarized as follows:

(1) Steady state with and without particle recycling has been achieved and compared. With particle recycling, atoms recycled from both the wall and the divertor plates are clearly observed. Without particle recycling, there is no atom at steady state before SMBI.

(2) Transport dynamics in the radial direction has been studied. With a constant injection flux of molecule density at the outermost boundary flux surface, neutral molecules and atoms propagate inwards continuously across the separatrix and penetrate about 4 cm inside

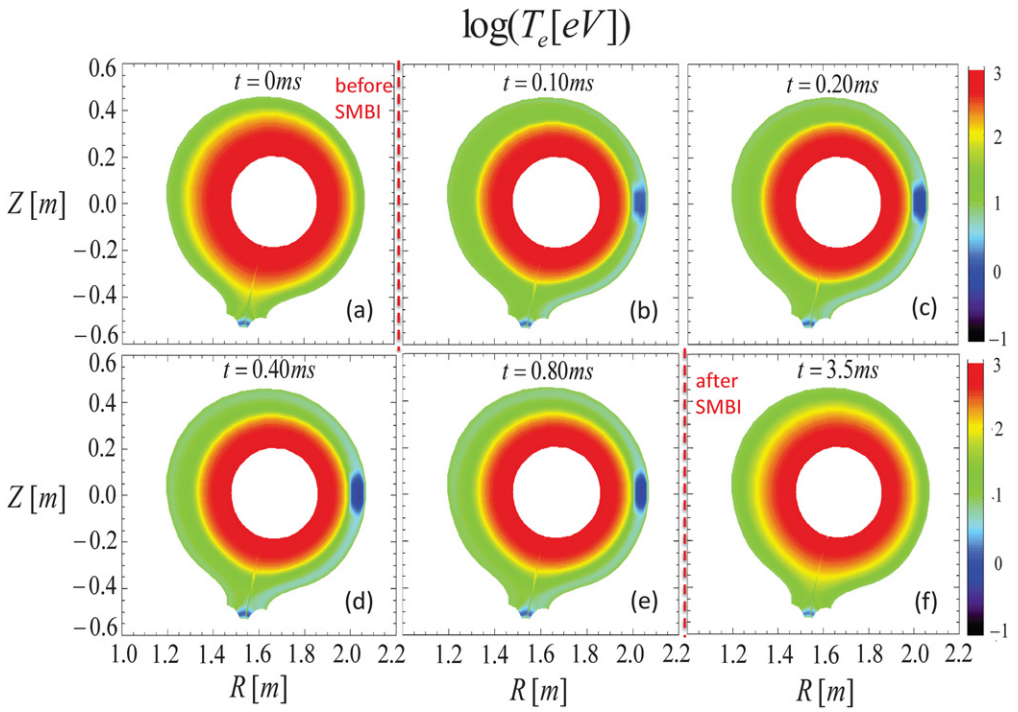

Figure 16. Poloidal hole of electron temperature sink keeps at the same location where SMB is injected once there is no electron heat convection, even though there is still parallel electron heat transport via electron thermal conductivity.

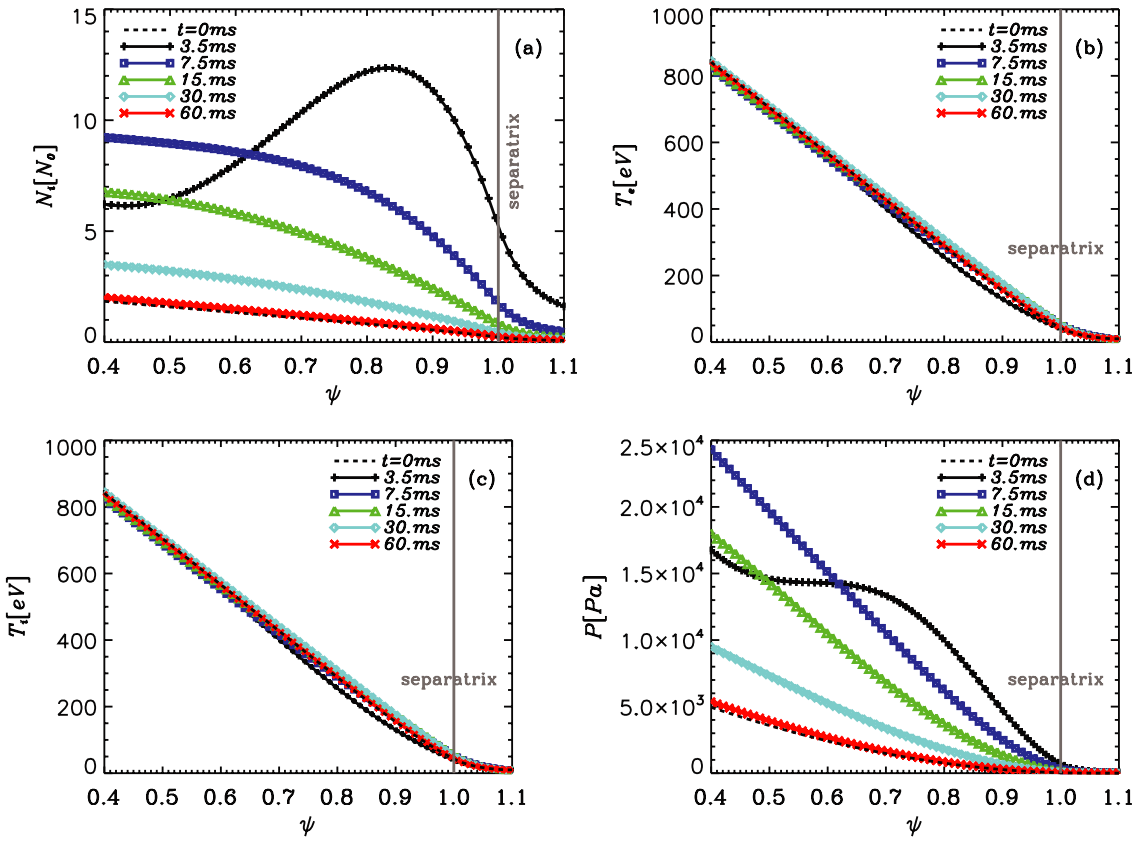

Figure 17. Time evolution of radial profiles relaxation after SMBI: (*a*) N_i, (*b*) T_e, (*c*) T_i and (*d*) P, which are plotted at outer mid-plane. Black dashed curves representing the initial time at steady state and black curves at the time when the system becomes uniform in poloidal direction.

the separatrix where the propagating front of molecules stagnates due to the total molecule dissociation rate balancing with the molecule injection rate at the SMBI source. Because the dissociation rate becomes larger as molecule penetrates deeper into the core of plasma, the molecular propagation speed becomes smaller and the propagating density front of molecules becomes steeper. Both locally peaked plasma density and locally decreased plasma temperature profiles are formed due to both particle fuelling and heat sinking effects of SMBI via neutrals dissociation and ionization. With continued SMBI, the local plasma density peak keeps increasing, leading to the total molecule dissociation rate becoming larger than the molecule injection rate. Subsequently, the molecular propagating front changes direction and moves outwards for a small step to reduce the local plasma density peak and also the total molecule dissociation rate. After that, the plasma density peak begins to increase again until the total molecule dissociation rate reaches the limit of being larger than the molecule injection rate and the outward movement continues. Thus, it has been observed that plasma density peak and neutrals fronts first propagating inwards continuously and then moving outwards step by step during SMBI. Once there is no SMBI, plasma density spreads outwards continuously and no step by step propagation is observed.

(3) Transport dynamics in the poloidal direction has also been studied. During SMBI, both locally peaked plasma density and locally dropped temperature profiles are observed in poloidal direction the same as in radial direction. Both positive and negative parallel ion velocities are driven near SMBI region due to parallel pressure gradient, which provides convection for poloidal transport of plasma density and ion temperature while poloidal transport of electron temperature depends on electron thermal conductivity only. Thus, the poloidal propagation of plasma density blobs (i.e. source) and ion temperature holes (i.e. sink) has been observed in both upward and downward directions in the cross-section of tokamak due to the convection of ion velocity. However, electron temperature holes keep at the same location without propagating poloidally when there is no electron convection included.

(4) After SMBI, the profiles of plasma density and temperatures become uniform in poloidal direction first via rapid poloidal transport while they are still relaxing in the radial direction towards the steady state. Plasma density increases while plasma temperatures decrease overall through the whole simulation domain. It takes about 2.5 ms for the system to become uniform in poloidal direction, while it takes much longer time, about 60 ms for it to relax back to its initial steady state.

These results then suggest several natural extensions of this work. They are the following:

(i) Further detailed studies of fuelling efficiency and penetration depth of SMBI by varying the molecule injection flux of SMBI. The penetration depth simply depends on the balance of SMBI rate and the total molecule dissociation rate. If the SMBI flux increases, the penetration depth should increase. For the same SMBI velocity and the same plasma conditions (i.e. N_i, T_e and T_i), the penetration depth should increase with an increase in SMBI density, while the penetration depth should increase with an increase in SMBI velocity for the same SMBI density. It should be very interesting to see the difference of the penetration depths for the same SMBI injection rates, but with a different injection velocity and density.

(ii) Further studies of a multi-scale problem of ELM mitigation during SMBI. Mean profile evolution is on the plasma transport time scale (∼tens of ms), while ELM events are on Alfven time scale (tens of μs). It is a challenge to simulate this multi-scale problem self-consistently, but it is also significant to understand the physics of tokamak plasmas occurring simultaneously on both scales. To do this with the BOUT++ code, it should couple the new *trans-neut* module dealing with neutrals and plasmas transport with another ELM-peeling/ballooning (elm-pb) module dealing with ELM dynamics. The previous module provides mean profiles for the second module while the second module provides feedback of turbulence to the previous module (i.e. turbulent diffusivities). The data communication between these two modules should be on a meso-scale, which is greater than Alfven time scale but smaller than the transport time scale.

(iii) Inclusion of additional equations of turbulence intensity transport [33, 34] and turbulent diffusivities in heat and particle transport equations to study mean profile evolutions during SMBI with self-consistent turbulent diffusivities. Also, the integration of a fundamentally non-local transport operator [35] into the heat evolution equation and a study of its impact on non-local [36] heat transport.

Acknowledgments

The authors wish to thank B.D. Dudson and M.V. Umansky for their contributions to BOUT++ framework and for X.R. Duan, A.K. Wang and Y. Liu for their support for US-China international collaboration project. Z.H. Wang also thanks P.W. Xi, B. Gui, I. Joseph, L.H. Yao, P.H. Diamond, W.W. Xiao, S.S. Kim, T. Rhee, J. Loizu, A. Dimits, W. Deng, J.Q. Xu, C.H. Ma for their fruitful physical discussions.

This work was supported by NSFC, Grant Nos 11205053 and 11261140326, and the US Department of Energy by Lawrence Livermore National Security, LLC, Lawrence Livermore National Laboratory under Contract DE-AC52-07NA27344. Z.H. Wang was also supported by China National Magnetic Confinement Fusion Science Program, Grant 2013GB111000, 2013GB107002, Chinese National Fusion Project for ITER Grant No 2013GB107000, and NSFC, Grant No 11205051. The LLNL IM release number of this manuscript is LLNL-JRNL-644017.

Appendix

Several simple analytical tests of the code have been done in 1D slab geometry against the analytical solutions of Burger's

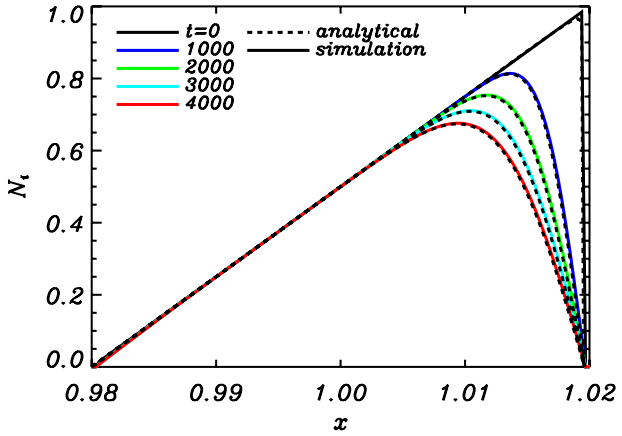

Figure A1. Normalized density profiles of simulation results (solid curves) and analytical results (dashed curves) at different times for 1D diffusion equation without source.

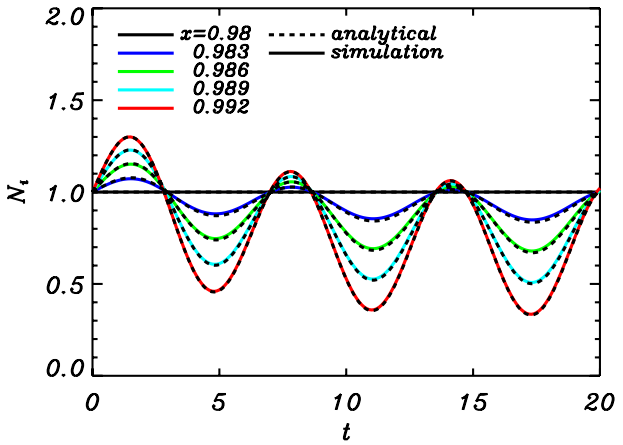

Figure A2. Time evolutions of normalized density of simulation results (solid curves) and analytical results (dashed curves) at different positions for 1D diffusion equation with source.

equation and diffusion equation with/without spatio-temporal varying source which are all consistent very well with each other.

(1) 1D diffusion equation without source
A simple 1D diffusion equation without source with initial and boundary conditions is

$$\begin{cases} \frac{\partial N_i}{\partial t} - D\frac{\partial^2 N_i}{\partial x^2} = 0, \\ N_i|_{x_0} = U_0, \quad N_i|_{x_1} = U_1, \\ N_i|_{t=0} = f(x). \end{cases} \tag{A1}$$

Its analytical solution [37] is

$$N_i(x,t) = U_0 + (U_1 - U_0)x' + \sum_{n=1}^{\infty} c_n \sin(n\pi x') e^{-D' n^2 \pi^2 t}, \tag{A2}$$

where $c_n = 2\int_0^1 f(x')\sin(n\pi x')\,dx' + (2/n\pi)((-1)^n U_1 - U_0)(n = 1, 2, 3\ldots)$, $x' = (x - x_0)/(x_1 - x_0)$ and $D' = D/(x_1 - x_0)$. In simulation, dimensionless parameters: $D = 1$, $x_0 = 0.98$, $x_1 = 1.02$ and $f(x) = (x - x_0)/(x_1 - x_0)$. The simulation result consists very well with the analytical solution given by equation (A2) as shown in figure A1.

(2) 1D diffusion equation with source
Another simple 1D diffusion equation with source with initial and boundary conditions is:

$$\begin{cases} \frac{\partial N_i}{\partial t} - D\frac{\partial^2 N_i}{\partial x^2} = C_0 x' \cos(t), \\ N_i|_{x_0} = 1, \quad N_i|_{x_1} = 0, \\ N_i|_{t=0} = 1, \end{cases} \tag{A3}$$

where, $x' = (x - x_0)/(x_1 - x_0)$.

Its analytical solution [37] is:

$$N_i(x,t) = 1 - x' + \sum_{n=1}^{\infty} c_n \sin(n\pi x') e^{-\lambda_n t}, \tag{A4}$$

where $c_n = 2C_0\cos(n\pi)(e^{\lambda_n t}(\lambda_n\cos(t) + \sin(t)) - \lambda_n)/n\pi(\lambda_n^2 + 1)(n = 1, 2, 3\ldots)$, $\lambda_n = D' n^2\pi^2$ and $D' = D/(x_1 - x_0)$. In simulation, dimensionless parameters: $D = 10000$, $C_0 = 1$, $x_0 = 0.98$ and $x_1 = 1.02$. The simulation result also consists very well with the analytical solution given by equation (A4) as shown in figure A2.

(3) Burger's equation
Consider the Burger's equation with initial and boundary conditions:

$$\begin{cases} \frac{\partial N_i}{\partial t} + N_i\frac{\partial N_i}{\partial x} - D\frac{\partial^2 N_i}{\partial x^2} = 0, \\ N_i|_{x=0} = 0, \quad N_i|_{x=1} = 0, \\ N_i|_{t=0} = 1, \end{cases} \tag{A5}$$

By the Hopf–Cole transformation

$$N_i = -2D\frac{\partial\omega/\partial x}{\omega}. \tag{A6}$$

The Burger's equation transforms to linear diffusion equation

$$\begin{cases} \frac{\partial\omega}{\partial t} - D\frac{\partial^2\omega}{\partial x^2} = 0, \\ \frac{\partial\omega}{\partial x}|_{x=0} = 0, \quad \frac{\partial\omega}{\partial x}|_{x=1} = 0, \\ \omega|_{t=0} = Ae^{-x/2D}, \end{cases} \tag{A7}$$

where A is an arbitrary constant. The analytical solution [37] of equation (A7) can be obtained

$$\omega(x,t) = c_0 + \sum_{n=1}^{\infty} c_n \cos(n\pi x) e^{-\lambda_n t}, \tag{A8}$$

where $\lambda_n = Dn^2\pi^2$, $c_0 = A\int_0^1 e^{-x/2D}\,dx$, and $c_n = 2A\int_0^1 e^{-x/2D}\cos(n\pi x)\,dx (n = 1, 2, 3\ldots)$.

Thus, using Holf–Cole transformation in equation (A6), the exact analytical solution to equation (A5) is obtained as:

$$N_i(x,t) = 2D\frac{n\pi\sum_{n=1}^{\infty} c_n \sin(n\pi x) e^{-\lambda_n t}}{c_0 + \sum_{n=1}^{\infty} c_n \cos(n\pi x) e^{-\lambda_n t}}. \tag{A9}$$

In simulation, dimensionless parameters: $D = 10$ and the simulation domain $x = [0.98, 1.02]$ is renormalized to $x = [0, 1]$ via $x = (x - x_0)/(x_1 - x_0)$ to compare with the analytical solution. It is found that the simulation result consists very well with the analytical solution given by equation (A9) as shown in figure A3.

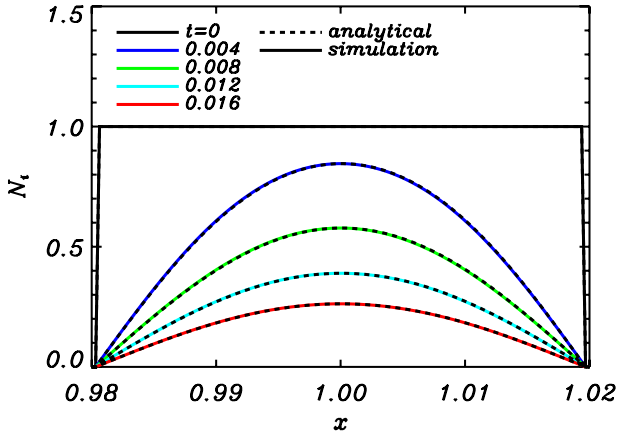

Figure A3. Normalized density profiles of simulation results (solid curves) and analytical results (dashed curves) at different times for 1D Burger's equation.

References

[1] Sajjad S., Gao X., Ling B., Bhatti S.H. and Ang T. 2009 *Phys. Lett.* A **373** 1133–9
[2] Baylor L.R. *et al* 2000 *Phys. Plasmas* **7** 1878
[3] Yao L.H. *et al* 2010 *Plasma Sci. Technol.* **12** 529
[4] Yu D.L. *et al* 2010 *Nucl. Fusion* **50** 035009
[5] Yu D.L. *et al* 2012 *Nucl. Fusion* **52** 082001
[6] Xiao W.W. *et al* 2010 *Phys. Rev. Lett.* **104** 215001
[7] Xiao W.W. *et al* 2012 *Nucl. Fusion* **52** 114027
[8] Sun H.J. *et al* 2010 *Plasma Phys. Control. Fusion* **52** 045003
[9] Parks P.B., Gerdin G.A., Vahala L.L. and Elcashlan A.G. 1994 *Nucl. Fusion* **34** 417
[10] Parks P.B. and Baylor L.R. 2005 *Phys. Rev. Lett.* **94** 125002
[11] Jiao Y.M., Zhou Y., Yao L.H. and Dong J.Q. 2003 *Plasma Phys. Control. Fusion* **45** 2001–10
[12] Xu X.Q., Nevins W.M., Cohen R.H., Rognlien T.D. and Umansky M.V. 2004 *Contrib. Plasma Phys.* **44** 105–10
[13] Rognlien T.D., Braams B.J. and Knoll D.A. 1996 *Contrib. Plasma Phys.* **36** 105
[14] Vold E.L., Najmabadi F. and Conn R.W. 1992 *Nucl. Fusion* **32** 1433
[15] Braginskii S.I. 1965 *Reviews of Plasma Physics* vol 1 ed M.A. Leontovich (New York: Consultants Bureau) p 205
[16] Simakov A.N. and Catto P.J. 2003 *Phys. Plasmas* **10** 4744
[17] Braams B.J. 1986 *Computational Studies in Tokamak Equilibrium and Transport* (Utrecht, Netherlands: State University)
[18] Rognlien T.D., Ryutov D.D., Mattor N. and Porter G.D. 1999 *Phys. Plasmas* **6** 1851
[19] Dudson B.D., Umansky M.V., Xu X.Q., Snyder P.B. and Wilson H.R. 2009 *Comput. Phys. Commun.* **180** 1467–80
[20] Xu X.Q., Umansky M.V., Dudson B. and Snyder P.B. 2008 *Commun. Comput. Phys.* **4** 949–79
[21] Umansky M.V., Xu X.Q., Dudson B., LoDestro L.L. and Myra J.R. 2009 *Comput. Phys. Commun.* **180** 887–903
[22] Xu X.Q., Cohen R.H., Rognlien T.D. and Myra J.R. 2000 *Phys. Plasmas* **7** 1951–8
[23] Landman I. and Janeschitz G.J. 2007 *Nucl. Mater.* **363–365** 1061
[24] Connor J.W., Hastie R.J., Wilson H.R. and Miller R.L. 1998 *Phys. Plasmas* **5** 2687
[25] Xu X.Q., Dudson B.D., Snyder P.B., Umansky M.V. and Wilson H.R. 2010 *Phys. Rev. Lett.* **105** 175005
[26] Xu X.Q., Dudson B.D., Snyder P.B., Umansky M.V., Wilson H. and Casper T. 2011 *Nucl. Fusion* **51** 103040
[27] Dudson B.D., Xu X.Q., Umansky M.V., Wilson H.R. and Snyder P.B. 2011 *Plasma Phys. Control. Fusion* **53** 054005
[28] Xi P.W., Xu X.Q., Wang X.G. and Xia T.Y. 2012 *Phys. Plasmas* **19** 092503
[29] Xia T.Y., Xu X.Q., Dudson B.D. and Li J. 2012 *Contrib. Plasma Phys.* **52** 353
[30] Xia T.Y. and Xu X.Q. 2013 *Phys. Plasmas***20** 052102
[31] Seaton M.J. 1959 Radiative recombination of hydrogenic ions *Mon. Not. R. Astron. Soc.* **119** 81
[32] Stangeby P.C. 2000 *The Plasma Boundary of Magnetic Fusion Devices (Plasma Phyiscs)* (London: Institute of Physics Publishing) p 717
[33] Gurcan O.D., Diamond P.H., Hahm T.S. and Lin Z. 2005 *Phys. Plasmas* **12** 032303
[34] Wang Z.H., Diamond P.H., Gurcan O.D., Garbet X. and Wang X.G. 2011 *Nucl. Fusion* **51** 073009
[35] Dif-Pradalier G, Diamond P.H., Grandgirard V., Sarazin Y., Garbet X., Abiteboul J., Ghendrih Ph., Strugarek A., Ku S. and Chang C.S. 2010 *Phys. Rev.* E **82** 025401(R)
[36] Sun H.J., Ding X.T., Yao L.H., Feng B.B., Liu Z.T., Duan X.R. and Yang Q.W. 2010 *Plasma Phys. Control. Fusion* **52** 045003
[37] Andrews L.C. and Phillips R.L. 2003 *Mathematical Techniques for Engineers and Scientists* (Bellingham, WA: SPIE Press)